Using ruptures from an earthquake cycle simulator to test geodetic early warning system performance

Margarita M. Solares-Colón[1], Diego Melgar[1], Andrew Howell[2], Brendan Crowell[3], Elisabetta D'Anastasio[2], Emmanuel Caballero[2], and Bill Fry[2]

[1]Department of Earth Sciences, University of Oregon, Eugene, Oregon, U.S.A.
[2] Earth Sciences New Zealand, Lower Hutt, Aotearoa, New Zealand
[3]School of Earth Sciences, The Ohio State University, Columbus, Ohio, U.S.A.

Corresponding author: M. M. Solares-Colón (msolares@uoregon.edu)

Author ORCIDs

Margarita M. Solares-Colón: 0000-0002-9387-7551
Diego Melgar: 0000-0001-6259-1852
Andrew Howell: 0000-0001-6858-4864
Brendan Crowell: 0000-0001-7096-601X
Elisabetta D'Anastasio: 0000-0003-3043-8604
Emmanuel Caballero: 0000-0002-2514-0670
Bill Fry: 0000-0003-3753-6928

Author contributions

Conceptualization: M. M. Solares-Colón, D. Melgar
Formal Analysis: M. M. Solares-Colón, D. Melgar, A. Howell,
Funding Acquisition: D. Melgar, B. Crowell, E. D'Anastasio, B. Fry
Investigation: M. M. Solares-Colón, D. Melgar, A. Howell
Methodology: M. M. Solares-Colón, D. Melgar, A. Howell, B. Crowell
Project Administration: D. Melgar, E. D'Anastasio, B. Fry
Resources: D. Melgar, A. Howell, B. Crowell, E. D'Anastasio, B. Fry
Supervision: D. Melgar
Validation: E. Caballero
Visualization: M. M. Solares-Colón, D. Melgar
Writing – original draft: M. M. Solares-Colón, D. Melgar
Writing – review & editing: M. M. Solares-Colón, D. Melgar, A. Howell, B. Crowell, E. D'Anastasio, E. Caballero, B. Fry

Abstract

New Zealand's vulnerability to seismic hazards highlights the need for systems capable of providing earthquake early warning (EEW) or rapid notice of strong shaking. Large offshore earthquakes along the subduction zone east of the North Island could also trigger catastrophic tsunamis, inundating coastal communities in under an hour. While New Zealand operates a robust seismic and geodetic network capable of monitoring moderate-to-large earthquakes, the limited observational record of large earthquakes poses challenges for EEW design and response. This study evaluates magnitude estimation from G-FAST, an early warning algorithm that uses Global Navigation Satellite System (GNSS) data to characterize earthquake sources. We analyze synthetic rupture scenarios along the Hikurangi subduction margin generated by the earthquake simulator RSQSim. For each rupture, GNSS displacements are generated at each site and compared with Peak Ground Displacement (PGD) scaling relationships to test whether they replicate real earthquakes. While we also assess PGD values from rupture scenarios produced with simpler semi-stochastic kinematic modeling, those from RSQSim yield ground motions more consistent with expected values. Given these results, synthetic displacement data from RSQSim ruptures were ingested into G-FAST to evaluate performance for rapid earthquake characterization, finding that PGD-based estimates capture moment magnitude in 90% of cases. This framework demonstrates the utility of synthetic catalogs for testing geodetic EEW performance in characterizing large subduction earthquakes in the North Island region and provides a pathway toward tsunami early warning procedures.

Resumen

La vulnerabilidad de Nueva Zelanda ante terremotos resalta la necesidad de contar con sistemas eficaces de alerta temprana. Terremotos de gran magnitud, especialmente en la zona de subducción al este de la Isla Norte, pueden desencadenar tsunamis catastróficos que afecten a comunidades costeras. Aunque el país cuenta con una red sísmica a tiempo real y geodésica continua capaz de monitorear terremotos moderados a grandes, la falta de registros de terremotos mayores representa un desafío. Este estudio evalúa el algoritmo de alerta temprana G-FAST, que utiliza datos del Sistema Global de Navegación por Satélite (GNSS) para caracterizar fuentes sísmicas. Analizamos escenarios de rupturas sintéticas generados por RSQSim, con distintas magnitudes y ubicaciones a lo largo del margen de subducción de Hikurangi. Para validar estos escenarios, se simularon desplazamientos en estaciones GNSS continuas y se compararon con relaciones de escala conocidas de desplazamiento máximo del suelo (PGD). También se evaluaron rupturas sintéticas generadas por un modelo cinemático semi-estocástico más simple, pero las rupturas de RSQSim produjeron desplazamientos más cercanos a los valores esperados. Luego examinamos el desempeño de G-FAST con los datos sintéticos de RSQSim , y se encontró que sus estimaciones basadas en PGD fueron precisas en el 90 % de los escenarios simulados. Este marco mejora la caracterización de grandes terremotos en Nueva Zelanda usando la red GNSS.

Plain Language Summary

New Zealand faces a high risk from earthquakes and tsunamis, with exposure across coastal areas of the North and South Islands. To reduce these risks, it is essential to have systems that can rapidly detect earthquakes and estimate their potential impact. A key challenge to designing these systems is the limited data from past large earthquakes, especially in the North Island, where large

earthquakes are most likely to occur offshore along the Hikurangi subduction zone. This study evaluates how well G-FAST, a computational tool that uses satellite-based Global Navigation Satellite Systems (GNSS) data, can quickly estimate the size of an earthquake. Because large earthquakes are rare, we used computer-generated scenarios to simulate a wide range of possible events along the Hikurangi region. To assess how realistic these simulations are, we created synthetic ground displacement data at continuous GNSS sites in New Zealand and compared them with established Peak Ground Displacement (PGD) models. PGD describes the maximum ground movement during an earthquake and is a key measure of earthquake intensity. Our results show that G-FAST can reliably estimate earthquake size in about 90% of simulated cases. This suggest the approach could significantly improve real-time earthquake monitoring and results presented in this study can support advancing tsunami early warning analysis for New Zealand North Island.

1.0 Introduction

Subduction zones are defined by deep trenches, where megathrust events are expected to rupture along the plate interface as stress accumulates over time. While these large earthquakes occur less frequently, they can trigger catastrophic tsunamis that impact coastal communities (e.g., the 2004 Indonesia, 2010 Maule, and 2011 Tohoku earthquakes; Lay et al., 2005; Mori et al., 2011; Vargas et al., 2011), leading to loss of life, structural damage, and other geological hazards such as ground failure. Because large events (**M** > 7) are comparatively rare, the instrumental record contains only limited near-source observations. This makes it difficult to test the effectiveness of rapid-response systems. To address this, researchers either reconstruct historical events (Ammon et al. 2005; Yue et al., 2014; Lay 2018) or generate synthetic rupture scenarios (Hok et al., 2011; Aguirre et al., 2018; Small & Melgar, 2023) to assess seismic and tsunami hazards in a region of interest. Here, we adopt the latter approach, using synthetic ruptures, which allow us to explore a

wider range of magnitudes and specifically test the response of an earthquake early warning (EEW) algorithm in areas where large events are scarce or have yet to occur.

For this study we focused on the Hikurangi subduction zone in New Zealand (**Figure 1**), which is located offshore east of the North Island of New Zealand at the southern end of the Kermadec-Tonga subduction system and defined as the boundary between the Pacific plate and the Australian plate. This region is considered an active seismic zone and capable of hosting large earthquakes (Clark et al., 2019; Wallace, 2020). Thus, coastal communities are vulnerable to seismic and tsunami hazards due to their proximity to the fault zone and topography in the area. At the southern end of the Hikurangi subduction margin it transitions into a strike-slip fault across the South Island. This is the Alpine Fault, a northeast-southwest striking dextral strike-slip fault in the west part of the South Island.

Given the potential for large subduction and crustal fault earthquakes, New Zealand is well equipped with a dense Global Navigation Satellite Systems (GNSS) network operated by GeoNet. A major multi-year public initiative led by GNS Science Te Pū Ao (now Earth Sciences New Zealand), the RCET (Rapid Characterization of Earthquakes and Tsunami) program, is exploring new techniques for rapid estimation of earthquake rupture characteristics in New Zealand. The RCET program is testing real-time and rapid-response algorithms, such as those used in geodetic EEW systems (for a comprehensive overview of GNSS-based warning, see Crowell (2024)). Here, we specifically want to assess the performance of the Geodetic First Approximation of Size and Timing (G-FAST; Crowell et al., 2016, Crowell et al., 2018), for rapid source characterization of moderate-to-large earthquakes using synthetic ruptures and geodetic data. Geodetic algorithms are desirable because traditional approaches that rely on inertial instruments, such as seismometers and accelerometers, can be biased by magnitude saturation and baseline offsets, respectively (refer

to review by Allen & Melgar, 2019). During an earthquake response, these factors could result in an inaccurate estimation of earthquake magnitude and an underestimation of seismic risks associated with the event. GNSS observations can address these issues but depend on the time required for slip to accumulate and for the signal to exceed the GNSS noise floor to detect an earthquake. For these reasons, we focus on evaluating large earthquakes ($\mathbf{M} \geq 7$) with geodetic data.

Due to the dearth of large earthquakes recorded with dense high-rate and real-time (HR) GNSS networks, the performance of geodetic EEW algorithms have been evaluated in previous studies using synthetic ruptures (e.g., Ruhl et al., 2017; Williamson et al., 2020; Nye et al., 2024). These approaches have relied on kinematic rupture models built using semi-stochastic simulations (e.g., LeVeque et al., 2016; Melgar et al., 2016), which represent "reduced-physics" approximations of the complexity of real large events. These models rely on statistical scaling laws and randomized slip generation techniques informed by historical finite-fault ruptures (e.g., Mai and Beroza, 2002; Melgar & Hayes, 2019). Kinematic parameterizations for rupture timing, velocity, and slip rate are then applied using empirical relationships from dynamic rupture simulations (e.g., Graves and Pitarka, 2010, 2015). In this study, we instead explore an earthquake catalog of megathrust rupture scenarios generated using a physics-based earthquake cycle simulator (**Figure 2**).

Physics-based simulators like the Rate and State Earthquake Simulator (RSQSim; Richards-Dinger & Dieterich, 2012) provide an alternative to these semi-stochastic methods for generating synthetic earthquake ruptures. RSQSim models the earthquake cycle over tens to hundreds of thousands of years using simplified frictional laws. Slip initiates and propagates in response to the evolving stress state on the fault, together with its frictional properties and

geometry, such that rupture extent, timing, and slip distributions emerge from physical processes and geometric complexity rather than imposed statistical assumptions. This approach enables the generation of complex events, such as joint subduction-crustal ruptures and multi-fault ruptures (Shaw et al., 2022; Delogkos et al., 2023), without imposing predefined rupture characteristics. These features suggest that RSQSim could serve as a valuable, and more physically consistent, alternative or complement to stochastic approaches—particularly in regions like New Zealand, where long-term deformation patterns are relatively well understood and geologic field data from paleoseismic records and slip rates are available. However, stochastic catalogs may remain preferable in contexts requiring a more comprehensive exploration of earthquake scenario variability (refer to **Figure S1** showing the spatial distribution and magnitude range of events from both catalogs).

The potential use cases of multi-cycle physics-based simulators for probabilistic seismic and tsunami hazard assessment have been highlighted by recent proof-of-concept studies (Shaw et al., 2018; Rafiei et al., 2022; Hughes et al., 2023). In this study, we evaluate whether synthetic earthquakes generated by RSQSim are sufficiently realistic to calibrate early warning systems. Specifically, we address the following questions: *(i) Are RSQSim-generated ruptures realistic enough for EEW testing applications? (ii) How do the ruptures from an earthquake simulator compare to ones generated by stochastic kinematic modeling? And (iii) How well does G-FAST perform in estimating the moment magnitude of these synthetic earthquake scenarios?* To investigate these questions, we first compute synthetic displacement time series at the current continuous (HR) GNSS stations in New Zealand (GNS Science, 2019) for each rupture scenario, assuming those were all high-rate and real-time. We then compare the synthetic observations against known Peak Ground Displacement (PGD) estimates from published ground-motion

models (GMMs) to validate our results. By applying this method, we can verify that these RSQSim ruptures mimic real earthquakes, at least to the extent that they produce realistic time-varying crustal deformation. We also perform the same PGD residual analysis using a second catalog of megathrust rupture scenarios, generated from semi-stochastic kinematic rupture models for the region of interest, to compare the results with those from an earthquake simulator. Finally, we ingest the synthetic GNSS data generated for RSQSim ruptures into an offline version of the G-FAST module in simulated real-time mode. G-FAST is an EEW module built for the ShakeAlert EEW system in the U.S. (Given et al., 2018) that rapidly estimates magnitude, moment tensor, and slip distribution of earthquakes using GNSS observations. Ultimately, we aim to assess how accurately G-FAST estimates the magnitude of these synthetic megathrust events using the current operating GNSS network in New Zealand. This study will advance the inclusion of HR-GNSS in earthquake and local tsunami warning systems in New Zealand by identifying areas of strong ground shaking that can be affected by an earthquake in the Hikurangi subduction zone, one of the largest sources of earthquake and tsunami hazard in New Zealand.

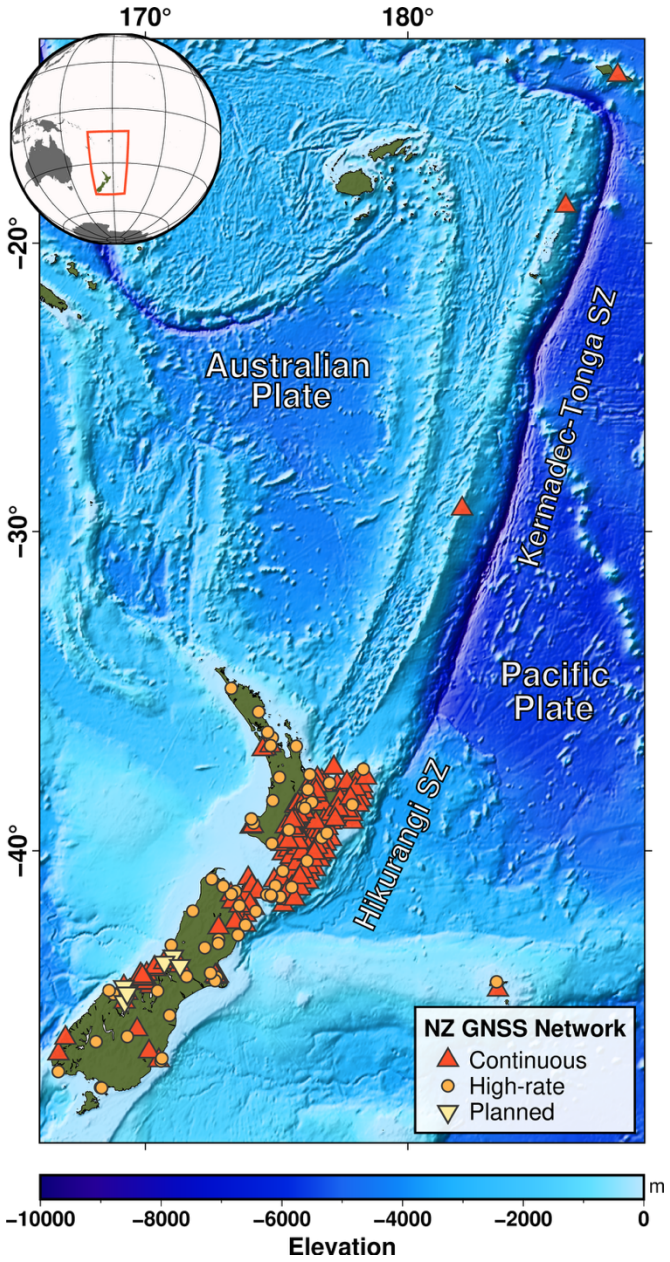

Figure 1. Tectonic Setting and Global Navigation Satellite System (GNSS) Network in New Zealand. Map highlighting the Kermadec-Tonga and Hikurangi subduction zones. The color-shaded relief represents bathymetry, with labeled plate boundaries for the Australian and Pacific plates. The station locations are indicated by red triangles for continuous GNSS stations (30s data), orange circles for high-rate continuous GNSS stations (1s data), and pale yellow triangles for planned stations. The inset globe provides geographic context, showing the study area in red.

2.0 Methods

In this section we detail the two approaches to rupture simulation, as well as the specifics of the waveform synthesis and EEW algorithm testing.

2.1 Finite-Rupture Models from an Earthquake Simulator

The first synthetic earthquake catalog of megathrust rupture scenarios was generated using RSQSim (Richards-Dinger & Dieterich, 2012), a quasi-static earthquake simulator that models long-term seismic cycles using rate-and-state friction laws (Dieterich, 1979). For reasons of computational efficiency, RSQSim simplifies the underlying fault physics more than modern multi-cycle earthquake simulators (Ozawa et al., 2022; Uphoff et al., 2022; Barbot, 2023; Zielke, 2023). Despite these simplifications, it can rapidly generate 10^5–10^6-year synthetic catalogs of earthquakes with slip distributions and magnitude–frequency characteristics that are realistic to first order.

We use synthetic ruptures from one of three synthetic earthquake catalogs generated by Hughes et al. (2025) for the Hikurangi-Kermadec subduction interface. This 30,000-year catalog includes 470 events ranging from **M**8.0 to **M**9.4 along the Hikurangi subduction zone (**Figure 2**). It uses the same subduction interface geometry as the New Zealand National Seismic Hazard Model 2022 Revision (NZSHM22; Gerstenberger et al., 2023), which was created by merging Slab 2.0 (Hayes, 2018) for the Kermadec portion with the Hikurangi interface geometry of Williams et al. (2013). Stressing rates and fault rake were derived from backslip loading, treating the geodetic slip-deficit rate distribution as representative of long-term slip in earthquakes (following Van Dissen et al., 2025). Following NZSHM22, present-day creeping sections were assumed not to host earthquake slip. We chose to use the "trench-locked" slip-deficit-rate

distribution (Hughes et al., 2025), mainly because we wished to include ruptures that slip to the trench but also because that was the preferred slip model of NZSHM22. In terms of frictional parameters, the rate-and-state a and b values were set at 0.001 and 0.004 respectively, to give average stress drops that match the magnitude-area scaling preferred by NZSHM22 (Stirling et al., 2024). The remaining frictional parameters used in RSQSim are provided in **Table S1** of the Supplementary Information and are discussed in detail by Hughes et al. (2025).

The earthquake simulator ruptures are "quasi-dynamic" because they do not resolve the full time history of slip at each subfault. Instead, it uses approximate rupture propagation governed by rate-and-state friction laws. In particular, slip-rate histories and rise times generated by RSQSim, required to describe the temporal evolution and duration of local slip on the fault, are not useful for our purposes — due to an assumption of constant rupture velocity by RSQSim. However, users can assign these parameters externally through kinematic assumptions when synthesizing waveforms. These are necessary to fully describe the rupture kinematics, and without them, it is not possible to generate waveforms directly from RSQSim ruptures. Following what is commonly done in kinematic rupture modeling, we can make some dynamically reasonable assumptions to add these parameters. We follow Graves & Pitarka (2010, 2015) to define rise times, where rise time scales with the square root of slip plus a magnitude scaling constant. As a result, patches with larger slip have longer rise times and larger ruptures have, on average, longer rise times as well. Additionally, each rise time receives a small stochastic perturbation so that similar amounts of slip have slightly different rise time values. For the slip-rate history, we assume the Dreger slip rate function. Mena et al., (2010) and Melgar et al. (2016) showed that this function has the appropriate spectral decay, compared to other common assumptions such as the triangle or raised cosine, and is consistent with rupture dynamics findings. The full details of this

implementation of rupture kinematics and how they have been modified from Graves & Pitarka (2010, 2015) for mega-thrust earthquakes is laid out in Melgar et al. (2016). Finally, with the full time history of each RSQSim rupture defined, we proceed to generate synthetic HR-GNSS data with FakeQuakes—which supports both rupture and waveform generation (described in the following sections), using a Green's function approach and velocity model from LITHO1.0 (Pasyanos et al., 2014).

2.2 Finite-Rupture Models from Semi-Stochastic Kinematic Modeling

The second synthetic catalog of megathrust rupture scenarios, used for comparison with RSQSim, was generated using FakeQuakes, part of the MudPy suite for semi-stochastic earthquake source modeling described by Melgar et al. (2016) and summarized herein. Statistical parameters in FakeQuakes have been calibrated to match those measured in slip distributions of global events (Melgar & Hayes, 2019) and a systematic comparison against large earthquakes has been carried out to validate that the resulting slip distributions represent what is seen in megathrust ruptures (Small & Melgar, 2023). The final catalog consists of 731 synthetic events with target magnitudes ranging from **M**7.8 to **M**9.4 along the Kermadec-Tonga subduction zone. To focus on the Hikurangi subduction region, the catalog was filtered to retain 381 events in which slip occurs at or south of 37.5°S.

To generate these rupture scenarios, we first defined the fault geometry as before, but with a coarser spatial resolution, and used the same 1-D velocity model from LITHO1.0, with a maximum depth of 25 km and a maximum slip of 50 m. The fault plane was discretized into a 3D mesh of subfaults, each assigned a displacement (slip vector) along the strike and dip directions. Stochastic rupture dimensions (length and width) were determined using the probabilistic scaling

laws of Blaser et al. (2010), with a randomly selected subfault as the hypocenter. Slip was distributed across the subfaults using a von Kármán correlation function, following the approach of Mai and Beroza (2002). This ensures consistency with the fault dimensions prescribed by the scaling laws to match the target magnitude. A Karhunen-Loève expansion (LeVeque et al., 2016) approach was then applied to model the spatial pattern of slip vectors, as it more accurately captures the complexity of observed earthquake slip distributions. From the resulting slip distribution, kinematic rupture parameters (i.e., rupture speed, rise time, and slip rate) were derived following the same methods used for the RSQSim ruptures in Section 2.1— recall that this follows from Graves and Pitarka (2010, 2015) and is calibrated to observations noted in Melgar et al. (2017). Finally, synthetic HR-GNSS data were generated with FakeQuakes, in a manner consistent with the RSQSim ruptures, using the same Green's function approach and velocity model.

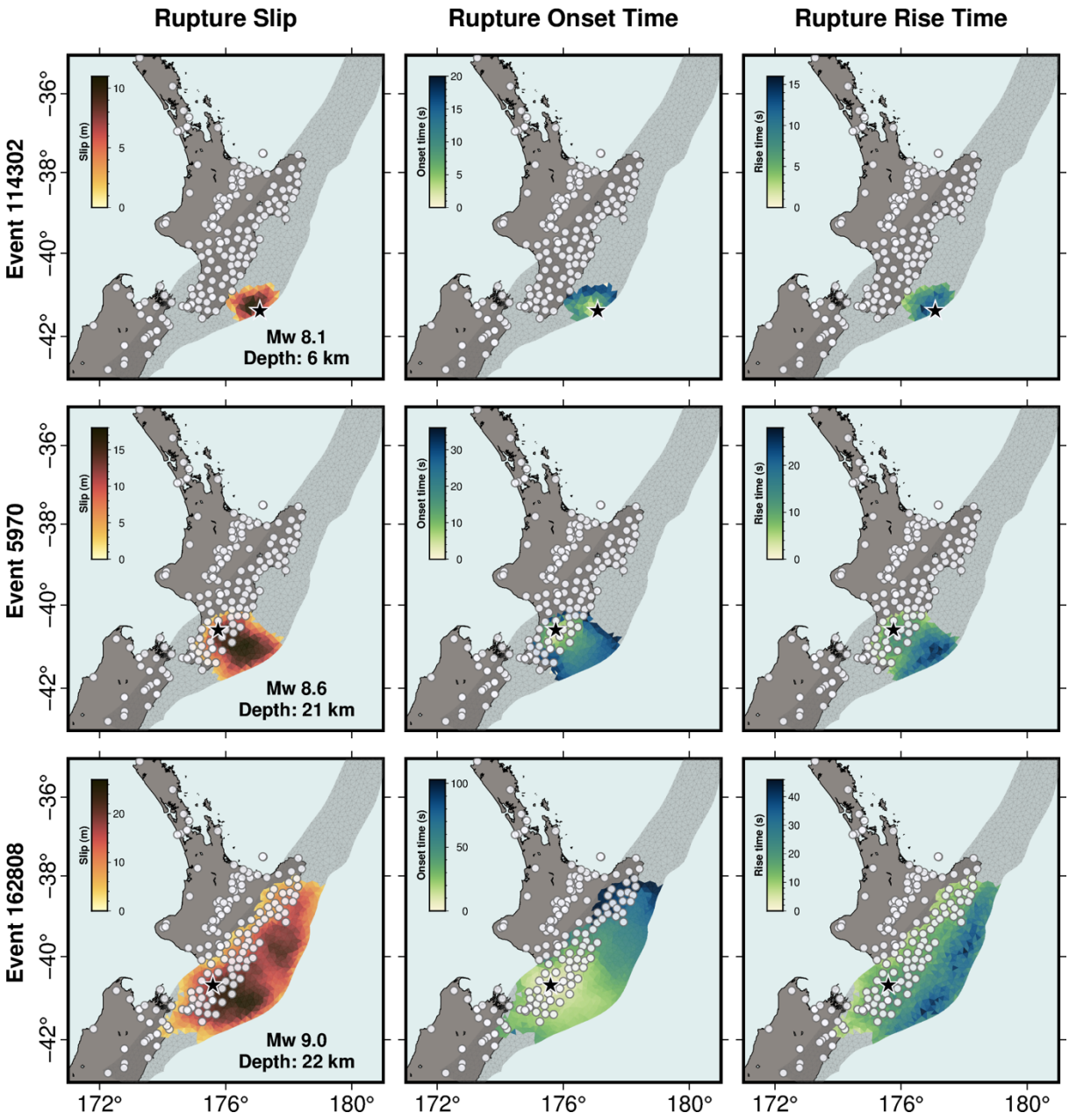

Figure 2. Three rupture scenarios generated by the RSQSim earthquake simulator. Rows represent individual events, and columns show: (1) rupture slip distribution, (2) rupture onset time, and (3) rise time for subfaults with slip greater than 10% of the maximum slip. White circles indicate the locations of GNSS stations, and the black star represents the event epicenter.

2.3 Generating synthetic HR-GNSS data

The GeoNet GNSS network provides dense station coverage across the North Island and sparser coverage in the South Island (GNS Science, 2019). In this study, to evaluate the

performance of G-FAST in New Zealand, we are using 239 existing continuous sites (including 56 high-rate stations delivering data in real-time), with an additional 6 sites planned for the South Island (**Figure 1**). Displacement data were synthesized for all stations using FakeQuakes. First, we calculated Green's functions using the method of Zhu and Rivera (2002) to obtain an impulse response for each station-subfault pair, thus relating ground motion at a site to slip on each subfault. We then convolved the Green's functions at each site with the slip-rate function of each sub-fault to synthesize waveforms at a sampling rate of 1Hz (**Figure 3c**). Finally, we obtained GNSS time series that represent ground motion at a specific site for all rupture scenarios in our catalog. To simulate realistic observations, random noise that simulates the power spectrum of real-time GNSS position noise was added to the synthetic GNSS displacement time series following Melgar et al. (2020)– this allows us to mimic instrumental errors and environmental variability. We used four different noise levels defined by Melgar et al. (2020), ranging from the 1st percentile (representing very low noise) to the 90th percentile (representing very high noise).

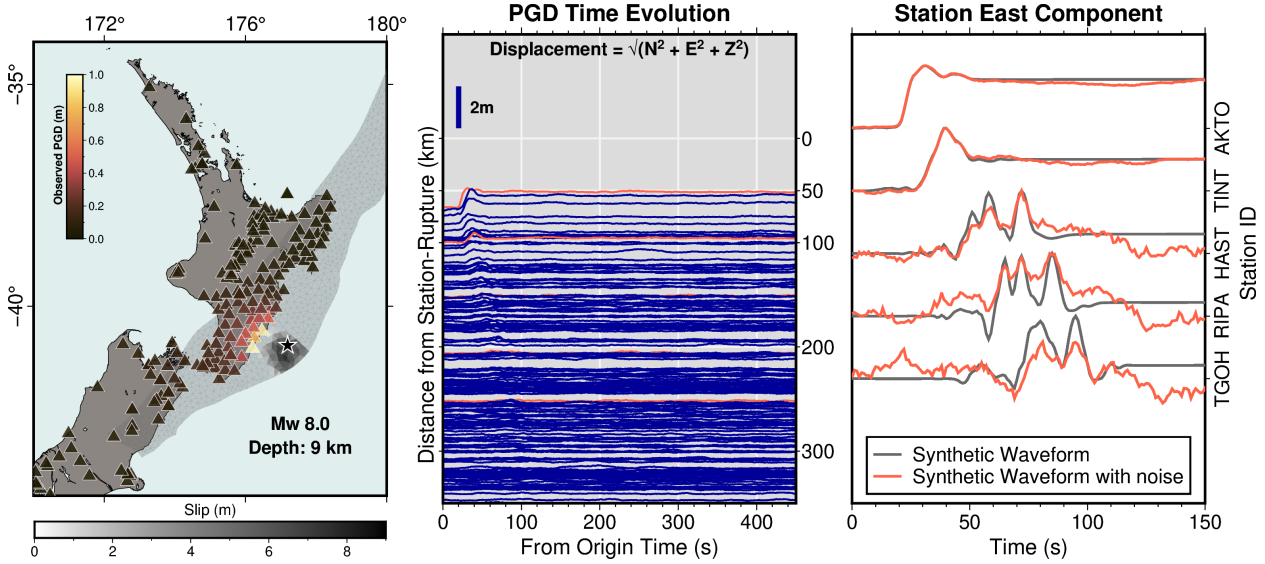

Figure 3. Synthetic high-rate Global Navigation Satellite System (HR-GNSS) data and waveforms. The left panel shows the observed peak ground displacement (PGD) values for a randomly selected rupture scenario, with slip distributions shown in grayscale for reference. The

center panel illustrates the time evolution of PGD for each station up to 350 km from the rupture; red lines indicate selected stations whose waveforms are shown in the right panel. The right panel presents synthetic waveforms with added noise examples.

2.4 Data validation

The GNSS Peak Ground Displacement (PGD) value is obtained from the root sum square of the three components in a GNSS time series that recorded the highest ground motion (**Figure 3**). This is a useful metric for estimating the size of an earthquake. In this study, we use the relation between PGD and moment magnitude to calculate the predicted PGD value at each GNSS station for every rupture scenario (Eq. 1). The GNSS Ground Motion Model (GMM) form is based on geodetic data and given by the following scaling law from Crowell et al. (2013):

$$log_{10}\,(PGD) = \mathrm{A} + \mathrm{B}\,\mathbf{M} + \mathrm{C}\,\mathbf{M}\,log_{10}(R)\,, \qquad \text{Eq. (1)}$$

where A, B, and C are the regression coefficients, **M** is the moment magnitude, and R is the distance between the GNSS station and the earthquake source (refer to **Table S2** of the Supplementary Information for coefficient values). To validate the GNSS waveforms in this study, we used a modified version of the GNSS GMM described above, incorporating the most recent regression coefficients and replacing the hypocentral distance with the generalized mean rupture distance (R_p; Thompson & Baltay, 2018), as implemented in Goldberg et al. (2021). R_p is the distance from the station to the entire rupture plane weighted by the slip (w) on each sub-fault (n) and raised to the power of the mean (p), express as follow:

$$R_p = \left(\sum_{i=0}^{n} w_i\, R_i^p\right)^{1/p}, \qquad \text{Eq. (2)}$$

with a value of p = -2.3, suitable for a wide range of rupture styles, as demonstrated in Goldberg (2021). The advantage of using R_p as a distance metric is that it allows for a more realistic treatment

of a finite source as opposed to assuming a large rupture is a point source (e.g. as with the hypocenter distance). The modified GNSS GMM model is calibrated using observed PGD measurements from 33 earthquakes world-wide of magnitude **M** 6-9, including the 2016 Kaikōura earthquake in New Zealand (for more details refer to Goldberg et al., 2021).

We calculated the residuals between the observed and predicted PGD values for each station and rupture using Equation 3. The observed values represent PGD from simulations, while the predicted values are derived from the modified GNSS GMM. To account for limitations in GMMs as we move away from the source, we filtered out PGD values for stations located more than 1000 km from the rupture. The residuals quantify how much the observed PGD deviates from the expected PGD for a given rupture scenario. This approach allows us to validate our results and assess whether RSQSim ruptures adequately simulate the behavior of real earthquakes.

$$\ln\left(\frac{PGD\ observed}{PGD\ predicted}\right), \qquad \text{Eq. (3)}$$

2.5 Testing EEW and rapid earthquake characterization

EEW systems are designed to provide rapid alerts of ground shaking by detecting initial seismic waves. Depending on the location and magnitude of the event, EEW systems can reduce the impact of earthquake hazards by alerting nearby communities, though warning times decrease as proximity to the source increases. The effectiveness of such systems depends on the network (station coverage), processing center (real-time data processing) and infrastructure (e.g., communications component to deliver alerts). Ultimately, the success of these systems is determined by how end-users receive, understand, and act on those alerts. Traditional EEW systems rely primarily on seismometers to estimate earthquake location and magnitude. In real-

time operation, G-FAST is triggered by seismic data, which provides an initial hypocenter, origin time, and magnitude of the event within seconds of seismic wave arrivals. G-FAST consists of three main modules: a first module that obtains the PGD to estimate a point-source magnitude, and a second module that computes a geodetic centroid moment tensor (gCMT) solution (Crowell et al., 2012) using the GNSS static offsets to determine fault orientations (strike and dip), location, and magnitude of the event (Crowell et al., 2013; Melgar, Crowell, et al., 2015; Crowell et al., 2018). From the gCMT nodal planes solution, a third module activates to invert for slip and produce a finite-fault model. For additional details about the operational version of G-FAST that is used within ShakeAlert, see Murray et al. (2023).

In this study, we use a modified offline version of G-FAST implemented in Python to process synthetic GNSS waveforms generated by FakeQuakes for the RSQSim ruptures, without relying on a seismic trigger. The production version of G-FAST was originally written in Python and later converted to C/C++, which is faster and more efficient for computing solutions. The hypocenter and magnitude from RSQSim rupture scenarios are used as the initial solution derived from seismic data. G-FAST begins with the first module to obtain PGD magnitude, as described in the previous section from Crowell (2013), and applies exponential weighting as a function of epicentral distance to prioritize stations closer to the source, using a minimum of four stations and a 3 km/s travel-time mask to exclude those that have not yet experienced strong ground shaking (Crowell et al., 2016). Subsequently, G-FAST estimates GNSS static offsets and initiates the second gCMT module. This module performs a grid search to find the optimal centroid location and invert for fault orientation. Lastly, G-FAST uses the nodal plane orientations from the gCMT solution to estimate finite-fault slip. The system runs for 480 s and produces a solution every second. We then evaluate its performance in reproducing the magnitudes of rupture scenarios

generated by RSQSim with the current operating GNSS network in New Zealand. We note that while G-FAST results could ultimately feed into EEW systems, this study does not test forecasting or alerting components. Instead, we focus on evaluating rapid source characterization using GNSS data. This approach aims to improve our understanding of earthquake processes in this region and, in combination with other complementary seismic EEW and rapid analysis tools (e.g. FinDer; Andrews et al., 2024), to better identify areas of strong ground shaking during future seismic events.

3.0 Results

Following is a description of the results with respect to validation for the GNSS waveforms and EEW performance.

3.1 Synthetic HR-GNSS data validation using catalog of megathrust ruptures scenarios

To validate our simulated data from synthetic ruptures, we performed a residuals analysis as defined in Equation 3. In this context, residuals indicate the discrepancies between the simulated (observed) PGD values and those predicted by the modified GNSS GMM. For example, a positive residual means that the observed PGD value is higher than expected, or that the GNSS GMM is underpredicting the PGD value, a negative residual signifies the opposite behavior. Ideally, we aim for residuals to behave such that, on average, they trend towards zero, which means that the observed and predicted values are in agreement, without biases correlated to event magnitudes or source-station distances. To investigate any biases in our simulations for accurately predicting ground motion, we plotted residuals against magnitude (teal) and rupture distance (brown) in **Figure 4**. Poor performance is expected at larger distances, where the PGD value tends to zero, and at lower magnitudes, where the signal falls below the noise floor.

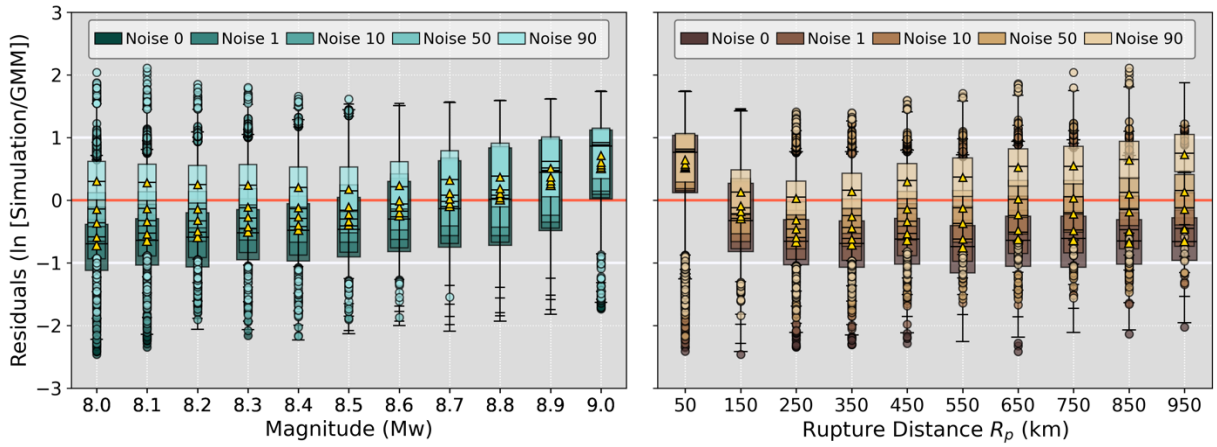

Figure 4. Boxplots of peak ground displacment (PGD) residuals for ruptures from the RSQSim catalog. The left panel shows residuals against magnitude (teal), while the right panel shows residuals against distance (brown). The red line represents zero, indicating the target residual value. Gold triangles denote the mean, and the horizontal black line represents the median per bin. The color shading corresponds to different Global Navigation Satellite System (GNSS) noise levels, ranging from the ideal scenario with no noise to the 90th percentile.

For this study, the synthetic HR-GNSS waveforms data were generated for an ideal scenario where all stations are functional and recording high-rate data continuously and in real-time. Given that the GMMs are derived from noisy data, we added noise to better approximate real-world conditions. In **Figure 4**, the boxplots represent the same dataset (i.e., PGD residuals using RSQSim rupture scenarios) but with increased noise levels. For the simulations, PGD values with no noise are lower than expected closer to -1 natural log unit, as shown in **Figure 4**. PGD values with no noise are critically underestimated at distances greater than ~150 km from the source to the station and for low to mid **M**8 events. Ultimately, we selected the 50th percentile over the 90th percentile, as the latter tends to overcorrect with positive residuals. The 50th percentile resulted in residuals closer to zero, aligning more closely with the predicted PGD values from the modified GNSS GMM (**Figure 4)**.

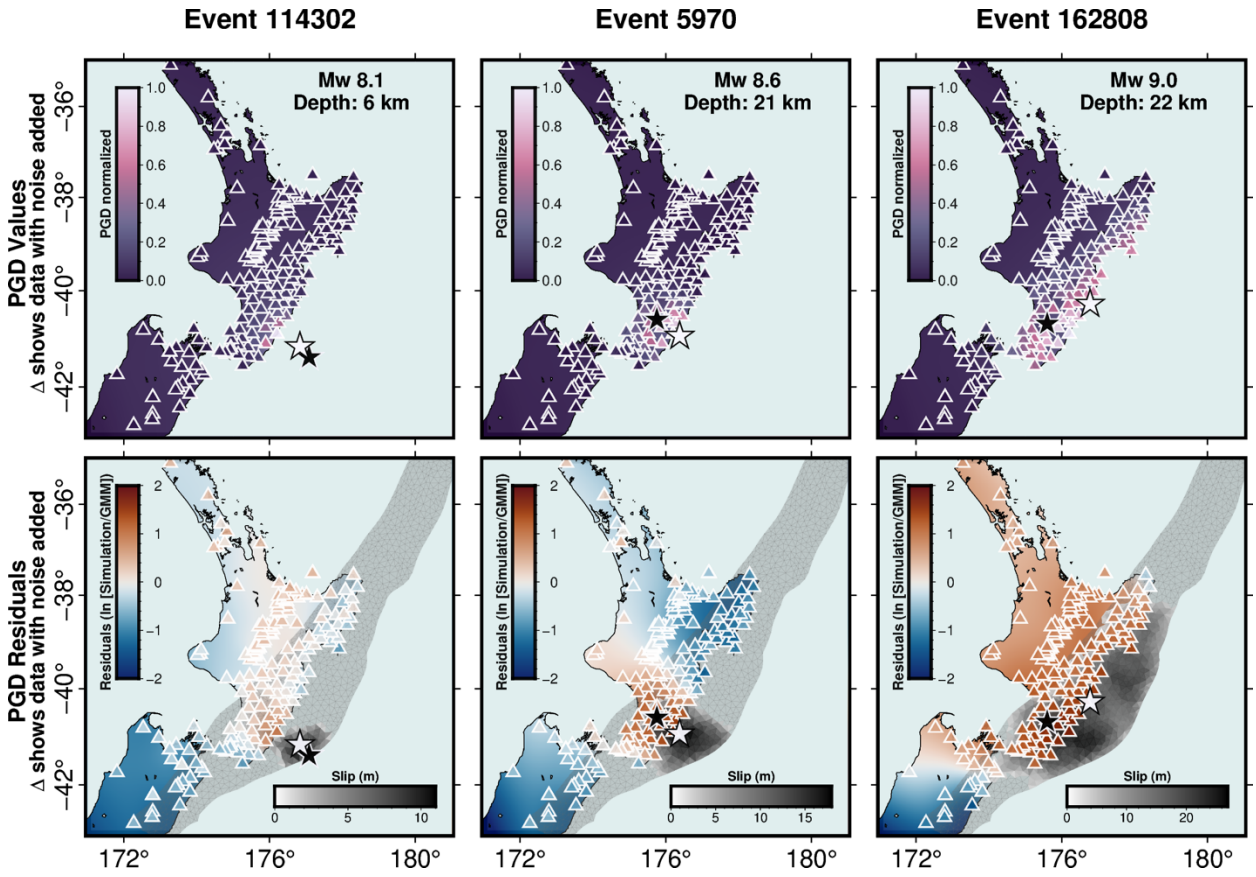

Figure 5. Spatial visualization of predicted and observed peak ground displacement (PGD) values and residuals for selected events. Each column represents a separate rupture scenario, with the black star indicating the hypocenter and the white star indicating the centroid location. The first row shows predicted PGD (surface grid) compared with observed PGD (color-filled triangles); labels indicate magnitude and depth of the event; vertical colormap indicates normalized PGD value. The second row shows PGD residuals without noise (surface grid) and PGD residuals with noise (color-filled triangles); vertical colormap indicates PGD resisdual and horizontal colormap indicates amount of slip for reference.

PGD results are shown for a set of RSQSim ruptures in **Figure 5** (same ruptures shown in **Figure 2**). The first row in **Figure 5** compares simulated PGD values with noise (triangles indicating station locations) to predicted PGD values from the GMP (surface interpolation) as groudtruth. We expect the colors to match, indicating that the simulated PGD values closely approximate the predicted PGD values. To better visualize the pattern, we normalized the PGD values. The colormap changes follow a similar pattern, highlighting the consistency between the

simulated and predicted PGD values. As anticipated, the highest PGD values are observed at stations near the earthquake source, primarily due to their proximity to the rupture. The second row in **Figure 5** compares the residuals of simulated PGD values with noise (triangles indicating station locations) to simulated PGD values without noise (surface interpolation) highlighting spatially how the added noise adjust lower-than-expected PGD values. For larger ruptures, the addition of noise has minimal impact. The noise added primarily helps adjust values that are lower than expected, as larger PGD values already exceed the noise threshold.

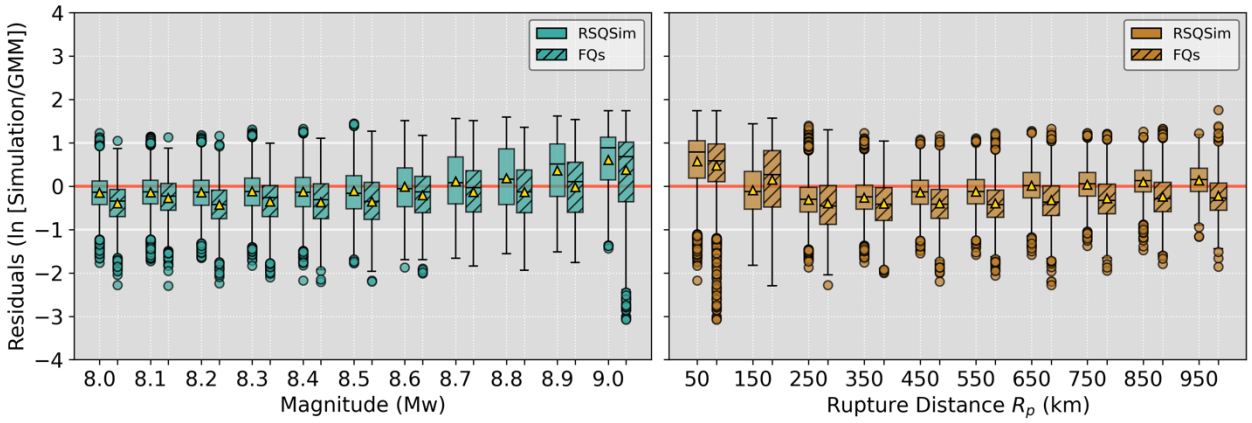

Figure 6. Boxplots of peak ground displacement (PGD) residuals for RSQSim ruptures (filled boxplots) and FakeQuakes ruptures (filled hatch boxplots). The left panel shows residuals against magnitude (teal), while the right panel shows residuals against distance (brown). The red line represents zero, indicating the target residual value. Gold triangles denote the mean, and the horizontal black line represents the median per bin.

In addition to generating synthetic waveforms, FakeQuakes module can also generate ruptures scenarios using a kinematic modeling approach, which is not necessarily physics-informed but is more computationally efficient compared to an earthquake simulator. Although FakeQuakes can produce a catalog with as many events as the user specifies, RSQSim generates an earthquake cycle that is arguably more representative of the long-term seismic behavior and fault interactions in a region. Therefore, we expect that ruptures from RSQSim will perform better

than those from FakeQuakes. We created a second synthetic catalog using FakeQuakes, with events in the **M**7.8 to **M**9.4 range targeted at the Hikurangi region, and generated synthetic waveforms to obtain PGD values. We then compared PGD residuals between RSQSim and FakeQuakes ruptures scenarios as shown in **Figure 6**. RSQSim ruptures (boxplots with solid fill color in **Figure 6**) generally yield residuals closer to zero than FakeQuakes ruptures (boxplots with solid fill and hatch in **Figure 6**), indicating better agreement with the expected PGD values from the modified GNSS GMM based on observed earthquakes. While both approaches rely on user-defined parameters, these results indicate that the RSQSim rupture scenarios more closely represent real earthquake behavior, as supported by their consistency with expected ground motions.

3.2 Performance of EEW magnitude estimates

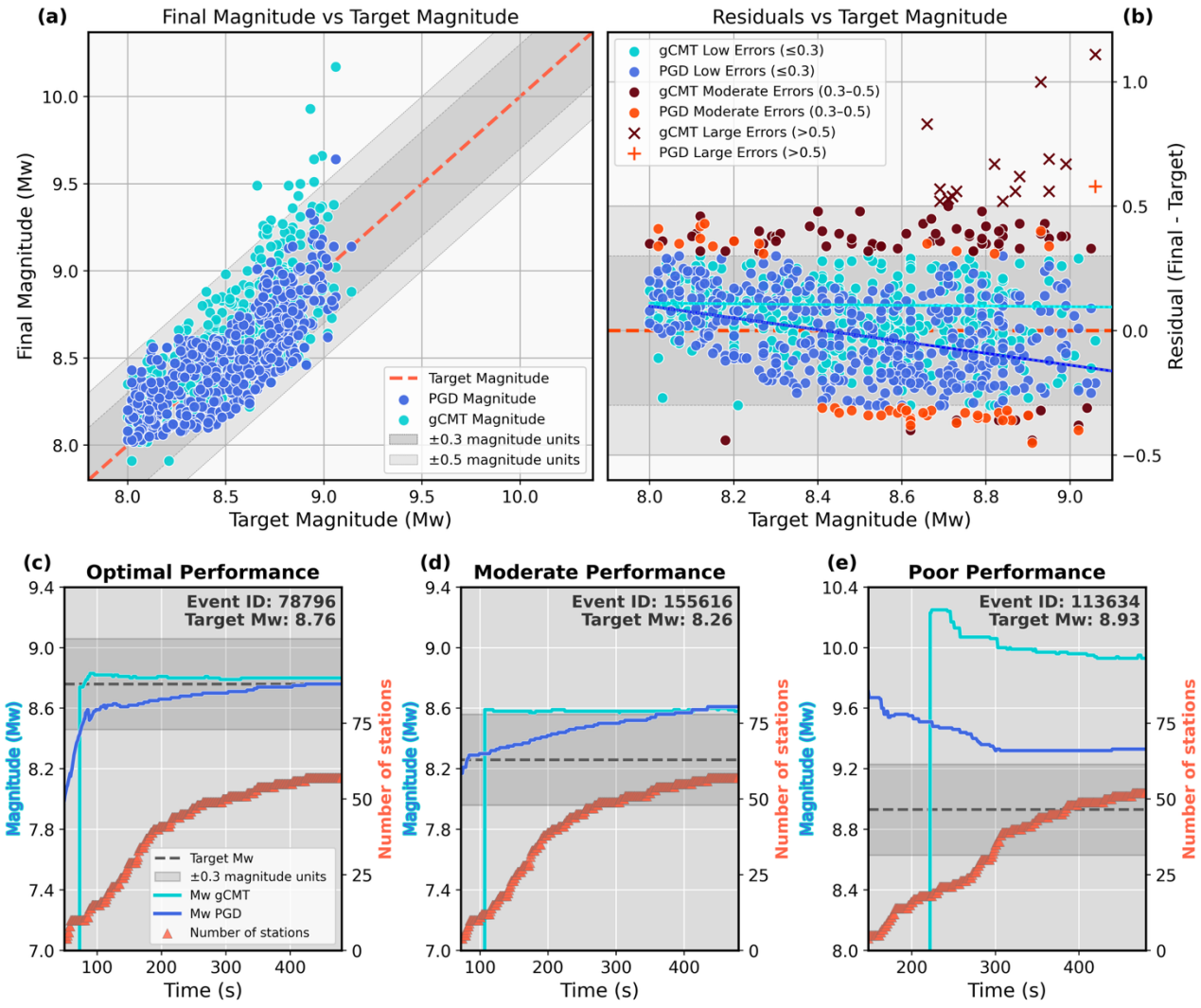

Figure 7. Comparison of G-FAST final magnitudes derived from peak ground displacement (PGD) and geodetic centroid moment tensor (gCMT) with target magnitudes for all rupture scenarios from RSQSim. Panel (a) shows PGD-derived magnitudes (blue) and gCMT-derived magnitudes (cyan) plotted against target magnitudes, with the red dashed line representing the true or target magnitude. Panel (b) shows magnitude residuals (Final – Target) for both PGD and gCMT modules, where markers highlight moderate errors (filled circles in warm colors) and large errors (symbols in warm colors). The red dashed line represents the zero residual baseline. In both panels, gray shaded regions indicate ±0.3 and ±0.5 magnitude deviations. Panels (c–e) illustrate examples of real-time magnitude evolution for three events demonstrating optimal (c), moderate (d), and poor (e) performance based on magnitude residuals. Each panel shows the time evolution of PGD (blue) and gCMT (cyan) magnitudes compared to the target magnitude (gray dashed line), along with the number of GNSS stations contributing to the solution (orangered). The gray shaded area represents ±0.3 magnitude deviations from the target.

We conducted a final test using synthetic GNSS waveforms generated by RSQSim to evaluate G-FAST's ability to estimate event magnitudes. In **Figure 7a**, we compare the PGD and gCMT magnitudes produced by G-FAST to the target magnitude (i.e., the synthetic moment magnitude) of each RSQSim event. Successful performance by G-FAST would yield magnitudes within the uncertainty bounds of ±0.3 magnitude units of the true magnitude. This threshold reflects the expected uncertainty of PGD-based magnitude estimates, as defined by Crowell et al., (2016). Estimates within this range provide reliable initial earthquake characterization, supporting downstream modeling such as tsunami forecasting (Williamson et al., 2020). To assess G-FAST's performance, we categorize the results into three groups as shown in **Figure 7b**: (1) optimal performance, where estimates fall within ±0.3 magnitude units (low errors); (2) moderate performance, where estimates fall between ±0.3 and ±0.5 magnitude units (moderate errors); and (3) poor performance, where errors exceed ±0.5 magnitude units (high errors). G-FAST correctly estimated magnitudes with optimal performance ~90% of the cases for PGD magnitude and ~81% for gCMT magnitude. The gCMT results appear more stable than the PGD magnitudes when following the linear trend (**Figure 7b**); however, they exhibit the largest errors, with 16 out of 17 events categorized as poor performance. In contrast, while the PGD results tend to underestimate the target magnitude, they are overall more accurate than the gCMT results, with lower errors.

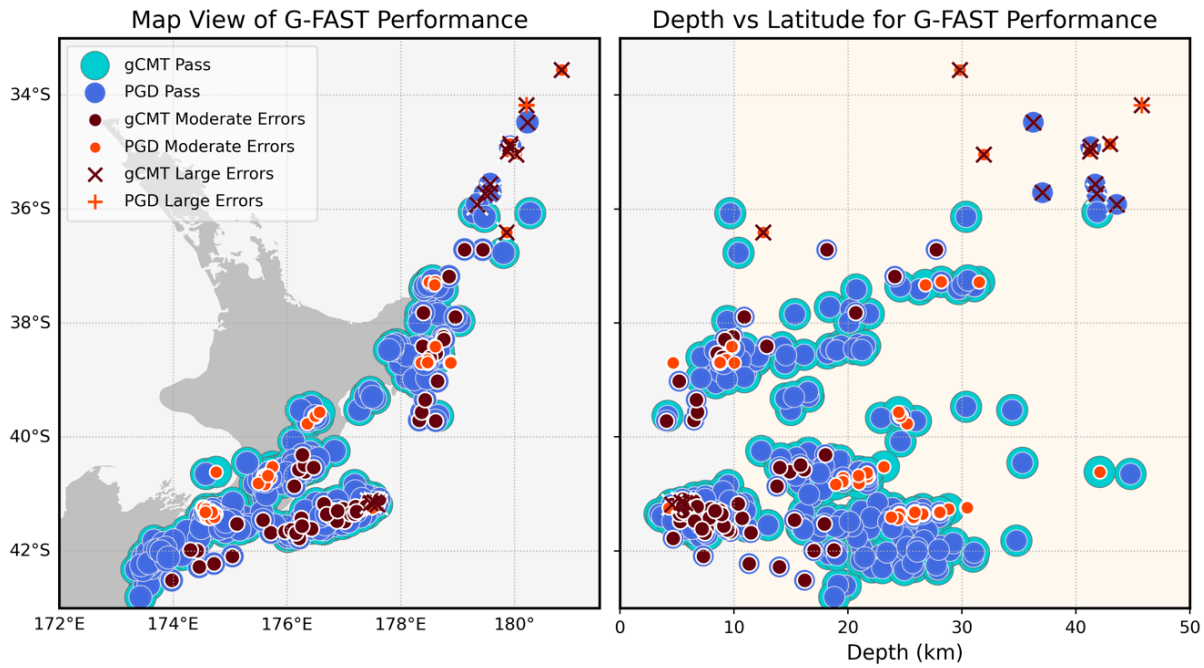

Figure 8. Spatial and depth distribution of G-FAST performance for all rupture scenarios from RSQSim. The left panel shows a map view of G-FAST performance, where peak ground displacement (PGD; blue) and geodetic centroid moment tensor (gCMT; cyan) solutions that pass the accuracy threshold are shown. Moderate errors (filled circles in warm colors) and large errors (symbols in warm colors) indicate discrepancies in magnitude estimation. The right panel shows depth vs. latitude distribution of G-FAST performance, illustrating the relationship between event depth and estimation accuracy. The same color scheme is used to distinguish passing solutions from those with moderate and large errors.

Events categorized as having poor performance were primarily associated with deeper hypocenters (≥30 km) located north of 36°S latitude (**Figure 8**). In most of these cases, the discrepancy between the hypocenter and centroid of the original rupture scenario was also large (**Figure 9** show discrepancies for PGD estimates and **Figure S2** in the Supplementary Information for the gCMT estimates). These ruptures propagated south, with slip concentrated south of the hypocenter, extending into the Hikurangi subduction zone. The exception is an event east of the North Island, near the edge of the Hikurangi margin towards the trench, which was a shallow event (~5 km depth). For events categorized as moderate performance, we note that if an event occurs near the station network with good coverage but at a depth of ~20 km or more for PGD results and

~10 km or more for gCMT results, G-FAST may not perform optimally in most cases. Meanwhile, the gCMT results are more scattered, particularly struggling at shallower depths and for sources located farther offshore.

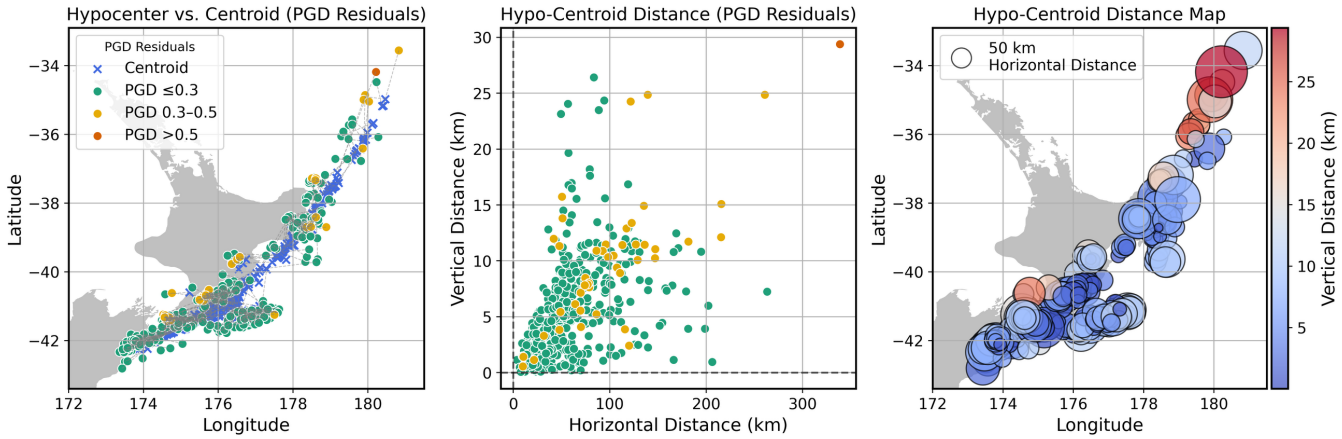

Figure 9. Comparison of hypocenter and centroid locations with magnitude residual (Final – Target) categories for peak ground displacement (PGD) solutions. The left panel shows hypocenter locations (circles) and centroid locations (blue crosses) for PGD residuals. Hypocenter locations are color-coded by error magnitude: green for low errors (≤0.3), yellow for moderate errors (0.3–0.5), and red for large errors (>0.5), corresponding to varying residual magnitudes. Centroid estimates from G-FAST are shown as white stars for comparison. The middle panel presents hypocenter vs. centroid locations for PGD residuals, following the same residual categorization. The right panel displays a hypocenter map, where marker size and color represent the horizontal and vertical distances, respectively, between the hypocenter and centroid.

An extraordinary case is a full rupture event in the Kermadec-Tonga subduction system, where G-FAST is unable to produce a solution (refer to **Figure S3** in the Supplementary Information). This occurs because the stations are too far from the epicenter to compute a reliable solution. Although this event does not necessarily occur in the Hikurangi subduction region, it shows substantial slip in this area, which could potentially cause strong ground shaking and/or pose a tsunami threat.

Discussion

This study provides a framework to evaluate G-FAST performance using simulations rather than real earthquakes and geodetic observations. As Earth Sciences New Zealand moves toward more timely and accurate earthquake characterization and tsunami forecasting, these simulations provide valuable insights into system behavior across a range of earthquake magnitudes and locations. Studies similar to the one presented here can help identify potential gaps in the current GNSS events that are more challenging to characterize, ultimately contributing to scientific strategies to improve future decision-making during an earthquake response.

First, we analyzed a catalog of megathrust rupture scenarios generated using the RSQSim earthquake cycle simulator, which demonstrated better performance than semi-stochastic kinematic rupture models (**Figure 6**). Before ingesting simulated GNSS waveforms from these rupture scenarios into G-FAST, we validated the synthetic displacement data against a modified GNSS-based GMM (Crowell et al., 2013; Goldberg et al., 2021) derived from earthquake data. This step ensured that the simulated data produced ground motions comparable to those observed from real earthquakes, as not every rupture results in 30 meters of displacement. To better reflect real-world conditions, we added noise to the synthetic GNSS waveforms, accounting for the inherently noisy geodetic data and improving the robustness of our results (**Figures 3 and 4**). This validation was essential, and further refinements could be made by incorporating real GNSS noise characteristics from the region into the generation of synthetic waveforms. However, for this exercise, the residuals remained within an acceptable range, supporting the reliability of our synthetic displacement data (**Figures 5 and 6**).

529 The optimal performance of G-FAST is defined here by its ability to estimate the target
530 magnitude within ±0.3 units for events (**Figure 7**), excluding one exceptional case involving a
531 full-margin rupture along the Kermadec–Tonga subduction zone, where the hypocenter was too
532 far from stations for G-FAST to resolve (**Figure S3**). Under this criterion, PGD estimation proves
533 to be a simple and reliable method, achieving this level of accuracy in 90% of rupture scenarios.
534 This is particularly notable when compared to Williamson (2018), who used a larger set of rupture
535 scenarios but with a stochastic modeling approach, achieving 82% accuracy in magnitude
536 estimation. However, the gCMT module's grid search could be improved, as it meets this threshold
537 in only 81% of cases and frequently fails to capture the true size of the event or select the correct
538 fault plane when using geodetic data alone. Factors contributing to moderate and poor G-FAST
539 magnitude estimate include the predominantly unilateral behavior of ruptures in the catalog, as
540 discussed by Williamson et al. (2020) and observed in this study (**Figure S2**). The imposed thrust
541 component, a characteristic of megathrust earthquakes, is prior knowledge that G-FAST does not
542 inherently account for and must instead resolve independently. If the rupture directivity propagates
543 in one direction, especially away from stations, it could create asymmetry in the observed PGD
544 values, where stations at similar distances from the source record different PGD values. This
545 variability could make it more challenging for a geodetic EEW system to resolve the rupture, as
546 seismic energy decays at larger distances, reducing the signal strength above the GNSS noise level
547 needed to detect an event or capture full slip distributions. Additionally, the complexity of the
548 rupture (e.g., multiple faults and asperities) further complicates event characterization. Other
549 contributing factors include the fact that many ruptures are one-sided, as the subduction interface
550 is offshore, and the high density of stations is located inland on the overriding plate. These
551 limitations highlight the need for a well-distributed and dense station network to improve event

552 characterization. While this is not a major concern in the North Island—except at greater depths
553 or farther offshore, it remains a constant challenge in subduction zone settings and other regions
554 of New Zealand such as the Alpine Fault where the station coverage is more sparce,

555 State-of-the-art tools using seismic data can provide accurate and timely information about
556 large earthquake magnitude and can encompass limitations of GNSS-HR techniques such as the
557 ones presented in this paper. But GNSS-HR is still an invaluable and unique tool to rapidly assess
558 the slip distributions of large events. This is provided by G-FAST and should be examined more
559 closely to validate slip in relation to the gCMT module and slip inversion. Accurately determining
560 magnitude is important but so is generating reliable slip models to gain deeper insight into rupture
561 processes and better inform tsunami warnings. Improving slip models would enhance our ability
562 to interpret rupture processes in real-time applications and better approximate ground motions and
563 tsunami hazards, which depend on the concentration of slip and the earthquake source. However,
564 both magnitude and slip estimates are sensitive to the initial earthquake location, which remains
565 fixed in this study but can introduce errors in real-time applications where depth is uncertain.
566 Building on this work, a forthcoming study (Caballero et al., in preparation) evaluates the impact
567 of depth uncertainty and grid search on the stability and accuracy of G-FAST solutions. The
568 framework presented here could also be extended to adapt the tsunami early warning approach
569 used in Williamson et al. (2020) to the Hikurangi subduction zone. Their study focused on near-
570 field tsunami forecasting in Cascadia using synthetic kinematic ruptures, and a similar
571 methodology could be tailored for Hikurangi with RSQSim-generated ruptures to assess tsunami
572 impact and complement offshore data (e.g., DART and tide gauge sensors). From this approach,
573 coastal amplitude thresholds for different tsunami sizes could be explored for integration into
574 tsunami forecasting systems. This has the potential to enhance the responsiveness of tsunami alerts

for coastal communities within the critical first few minutes after an earthquake, bridging the gap between earthquake detection and tsunami arrival, as demonstrated by Williamson et al. (2020).

Having focused on megathrust events, our framework could also be applied to other fault types. Crustal faults, for example, pose significant geological hazards – including landslides and strong ground shaking, depending on the timing and location of the earthquake. In the future, it would be valuable to explore more complex scenarios, such as the Alpine and Wellington faults, which both exhibit dextral motion with a dip component. The Alpine Fault, given its more remote location and potential to host **M**7-8 earthquakes (Orchiston et al., 2018; Howarth et al., 2021), may be better suited for rapid characterization of the source. In contrast, the Wellington Fault, located near densely populated areas, presents greater challenges for rapid response due to short source-to-site distances but offers an opportunity to test earthquake response strategies and identify zones of intense ground motion. Simulations of even more complex rupture scenarios, such as the multi-segment 2016 **M**7.8 Kaikōura rupture that extended offshore (Duputel & Rivera, 2017; Hamling, 2020), could also provide further insights, particularly when compared against real earthquake observations from GNSS records.

5.0 Conclusions

Are the ruptures generated by RSQSim realistic? Yes, to some extent. RSQSim ruptures mimic real earthquakes, validated using PGD as a metric to simulate ground motion and compare it to expected values from global earthquake statistics. *How do these ruptures compare to those produced by kinematic modeling*? RSQSim ruptures outperform kinematic modeling approach, which lack the (simple) physics-based constraints provided by earthquake simulators. *How well does G-FAST perform in estimating the moment magnitude of these synthetic earthquake*

scenarios? Overall, PGD magnitude estimation demonstrates high reliability, outperforming gCMT-based estimates by providing accurate magnitudes in most rupture scenarios—assuming ideal conditions where all stations are operational. Further evaluation of the gCMT grid search and spatial slip distribution is needed for a comprehensive assessment of G-FAST's performance and its implementation in New Zealand. In brief, rupture scenarios generated by earthquake simulators are a valuable tool for assessing seismic and tsunami hazards associated with potential earthquakes in regions of interest (Crowell et al., 2016; Williamson et al., 2020; Hughes et al., 2024). They also provide a testing ground for implementing rapid earthquake characterization algorithms within regional seismic networks for rapid response and early warning purposes, particularly for large earthquakes, where prior knowledge is limited due to long recurrence intervals and/or data availability. In this study, we leveraged the dense GNSS network in North Island of New Zealand to showcase our approach by generating synthetic data for rupture scenarios that allow us to characterize earthquakes and understand how ground motion can impact different areas based on proximity to source. For this study, we utilized HR-GNSS synthetic observations, which have been shown to complement seismic data by avoiding saturation at larger magnitudes (Crowell et al., 2013; Melgar et al., 2015). This integration enhances our ability to analyze and assess seismic and tsunami hazards, further advancing our understanding of earthquake behavior and its impacts in the region of interest. As more data sources are available, better decisions can be made during an earthquake response in a timely manner to save lives.

Acknowledgments

We would like to express our gratitude to Earth Sciences New Zealand (formerly known as GNS Science Te Pū Ao) for providing the resources and support necessary for this research. A. Howell, E. D'Anastasio, E. Caballero and B. Fry are supported by New Zealand Ministry of Business,

Innovation and Employment contract C05X2003 for the Rapid Characterization of Earthquakes and Tsunami (RCET) program. We also recognize funding from Aotearoa New Zealand National Tsunami Model support for B. Fry and the Natural Hazards Research Platform for support of Howell and Fry. The GeoNet GNSS network is sponsored by the New Zealand Government through its agencies: Natural Hazards Commission Toka Tū Ake (NHC), Earth Sciences New Zealand, Toitū Te Whenua Land Information New Zealand (LINZ) and the Ministry of Business, Innovation and Employment (MBIE). Finally, we thank Anna Kaiser, the editor Mathilde Radiguet, and two anonymous reviewers for their time and thoughtful comments, which helped improve the quality of this manuscript.

Data and Code Availability

Rupture models from both catalogs (RSQSim and FakeQuakes) and the simulated GNSS waveforms used in this study are publicly available in a Zenodo repository (Solares-Colón et al., 2025). FakeQuakes, which is part of the MudPy suite for source modeling, is available at https://github.com/UO-Geophysics/MudPy (release v1.3) and is also linked to our Zenodo repository. Additional scripts used to convert RSQSim outputs into FakeQuakes inputs for generating synthetic GNSS waveforms are available at https://github.com/mmsolares/rsqsim2fakequakes-tools . Figures were produced using the Python packages Matplotlib (Hunter, 2007), Obspy (Beyreuther et al., 2010), and PyGMT (Tian et al., 2024).

Competing interests

The authors declare no competing interests.

References

Aguirre, P., Vásquez, J., De La Llera, J. C., González, J., & González, G. (2018). Earthquake damage assessment for deterministic scenarios in Iquique, Chile. *Natural Hazards, 92*(3), 1433–1461. https://doi.org/10.1007/s11069-018-3258-3

Allen, R. M., & Melgar, D. (2019). Earthquake early warning: Advances, scientific challenges, and societal needs. *Annual Review of Earth and Planetary Sciences, 47*(1), 361–388. https://doi.org/10.1146/annurev-earth-053018-060457

Ammon, C. J., Ji, C., Thio, H.-K., Robinson, D., Ni, S., Hjorleifsdottir, V., Kanamori, H., Lay, T., Das, S., Helmberger, D., Ichinose, G., Polet, J., & Wald, D. (2005). Rupture process of the 2004 Sumatra-Andaman earthquake. *Science, 308*(5725), 1133–1139. https://doi.org/10.1126/science.1112260

Andrews, J., Behr, Y., Böse, M., Massin, F., Kaiser, A., & Fry, B. (2024). Rapid earthquake rupture characterization for New Zealand using the FinDer algorithm. *Bulletin of the Seismological Society of America, 114*(2), 775–793. https://doi.org/10.1785/0120230213

Barbot, S. (2023). Motorcycle: A spectral boundary-integral method for seismic cycles on multiple faults. *Journal of Open Source Software, 8*(91), 5097. https://doi.org/10.21105/joss.05097

Beyreuther, M., Barsch, R., Krischer, L., Megies, T., Behr, Y., & Wassermann, J. (2010). ObsPy: A Python toolbox for seismology. *Seismological Research Letters, 81*(3), 530–533. https://doi.org/10.1785/gssrl.81.3.530

Blaser, L., Kruger, F., Ohrnberger, M., & Scherbaum, F. (2010). Scaling relations of earthquake source parameter estimates with special focus on subduction environment. Bulletin of the Seismological Society of America, 100(6), 2914–2926. https://doi.org/10.1785/0120100111

Clark, K., Howarth, J., Litchfield, N., Cochran, U., Turnbull, J., Dowling, L., Howell, A., Berryman, K., & Wolfe, F. (2019). Geological evidence for past large earthquakes and tsunamis along the Hikurangi subduction margin, New Zealand. *Marine Geology, 412*, 139–172. https://doi.org/10.1016/j.margeo.2019.03.004

Crowell, B. W., Melgar, D., Bock, Y., Haase, J. S., & Geng, J. (2013). Earthquake magnitude scaling using seismogeodetic data. *Geophysical Research Letters, 40*(23), 6089–6094. https://doi.org/10.1002/2013GL058391

Crowell, B. W., Schmidt, D. A., Bodin, P., Vidale, J. E., Gomberg, J., Hartog, J. R., Kress, V. C., Melbourne, T. I., Santillan, M., Minson, S. E., & Jamison, D. G. (2016). Demonstration of the Cascadia G-FAST geodetic earthquake early warning system for the Nisqually, Washington, earthquake. *Seismological Research Letters, 87*(4), 930–943. https://doi.org/10.1785/0220150255

Crowell, B. W., Schmidt, D. A., Bodin, P., Vidale, J. E., Baker, B., Barrientos, S., & Geng, J. (2018). G-FAST earthquake early warning potential for great earthquakes in Chile. *Seismological Research Letters, 89*(2A), 542–556. https://doi.org/10.1785/0220170180

Crowell, B. W. (2024). Earthquake and tsunami early warning with GNSS data. In *GNSS monitoring of the terrestrial environment* (pp. 111–127). Elsevier. https://doi.org/10.1016/B978-0-323-95507-2.00004-9

Delogkos, E., Howell, A., Seebeck, H., Shaw, B. E., Nicol, A., Liao, Y. M., & Walsh, J. J. (2023). Impact of variable fault geometries and slip rates on earthquake catalogs from physics-based simulations of a normal fault. *Journal of Geophysical Research: Solid Earth, 128*(11), e2023JB026746. https://doi.org/10.1029/2023JB026746

Dieterich, J. H. (1979). Modeling of rock friction: 1. Experimental results and constitutive equations. *Journal of Geophysical Research: Solid Earth, 84*(B5), 2161–2168. https://doi.org/10.1029/JB084iB05p02161

Duputel, Z., & Rivera, L. (2017). Long-period analysis of the 2016 Kaikoura earthquake. *Physics of the Earth and Planetary Interiors, 265*, 62–66. https://doi.org/10.1016/j.pepi.2017.02.004

Gerstenberger, M. C., Bora, S., Bradley, B. A., DiCaprio, C., Kaiser, A., Manea, E. F., Nicol, A., Rollins, C., Stirling, M. W., Thingbaijam, K. K. S., Van Dissen, R. J., Abbott, E. R., Atkinson, G. M., Chamberlain, C., Christophersen, A., Clark, K., Coffey, G. L., de la Torre, C. A., Ellis, S. M., Fraser, J., Graham, K., Griffin, J., Hamling, I. J., Hill, M. P., Howell, A., Hulsey, A., Hutchinson, J., Iturrieta, P., Johnson, K. M., Jurgens, V. O., Kirkman, R., Langridge, R. M., Lee, R. L., Litchfield, N. J., Maurer, J., Milner, K. R., Rastin, S., Rattenbury, M. S., Rhoades, D. A., Ristau, J., Schorlemmer, D., Seebeck, H., Shaw, B. E., Stafford, P. J., Stolte, A. C., Townend, J., Villamor, P., Wallace, L. M., Weatherill, G., Williams, C. A., & Wotherspoon, L. M. (2023). The 2022 Aotearoa New Zealand National Seismic Hazard Model: Process, overview, and results. *Bulletin of the Seismological Society of America, 114*(1), 7–36. https://doi.org/10.1785/0120230182

Given, D. D., Allen, R. M., Baltay, A. S., Bodin, P., Cochran, E. S., Creager, K., de Groot, R. M., Gee, L. S., Hauksson, E., Heaton, T. H., Hellweg, M., Murray, J. R., Thomas, V. I., Toomey, D., & Yelin, T. S. (2018). *Revised technical implementation plan for the ShakeAlert system—An earthquake early warning system for the West Coast of the United States* (Open-File Report No. 2018-1155). U.S. Geological Survey. https://doi.org/10.3133/ofr20181155

GNS Science. (2019) [Dataset]. GeoNet Aotearoa New Zealand Stations Metadata Repository [Data set]. GNS Science, GeoNet. https://doi.org/10.21420/0VY2-C144

Goldberg, D. E., Melgar, D., Hayes, G. P., Crowell, B. W., & Sahakian, V. J. (2021). A ground-motion model for GNSS peak ground displacement. *Bulletin of the Seismological Society of America, 111*(5), 2393–2407. https://doi.org/10.1785/0120210042

Graves, R. W., & Pitarka, A. (2010). Broadband ground-motion simulation using a hybrid approach. *Bulletin of the Seismological Society of America*, 100(5A), 2095–2123. https://doi.org/10.1785/0120100057

Graves, R., & Pitarka, A. (2015). Refinements to the Graves and Pitarka (2010) broadband ground-motion simulation method. *Seismological Research Letters*, 86(1), 75–80. https://doi.org/10.1785/0220140101

Hamling, I. J. (2020). A review of the 2016 Kaikōura earthquake: Insights from the first 3 years. *Journal of the Royal Society of New Zealand, 50*(2), 226–244. https://doi.org/10.1080/03036758.2019.1701048

Hayes, G. (2018). *Slab2—A comprehensive subduction zone geometry model* [Dataset]. U.S. Geological Survey data release. https://doi.org/10.5066/F7PV6JNV

Hok, S., Fukuyama, E., & Hashimoto, C. (2011). Dynamic rupture scenarios of anticipated Nankai-Tonankai earthquakes, southwest Japan. *Journal of Geophysical Research, 116*(B12), B12319. https://doi.org/10.1029/2011JB008492

Howarth, J. D., Barth, N. C., Fitzsimons, S. J., & others. (2021). Spatiotemporal clustering of great earthquakes on a transform fault controlled by geometry. *Nature Geoscience, 14*(4), 314–320. https://doi.org/10.1038/s41561-021-00721-4

Hughes, L., Power, W., Lane, E. M., Savage, M. K., Arnold, R., Howell, A., Shaw, B., Fry, B., & Nicol, A. (2023). A novel method to determine probabilistic tsunami hazard using a physics-based synthetic earthquake catalog: A New Zealand case study. *Journal of Geophysical Research: Solid Earth, 128*(12), e2023JB027207. https://doi.org/10.1029/2023JB027207

Hughes, L., Lane, E. M., Power, W., Savage, M. K., Arnold, R., Howell, A., Liao, Y.-W. M., Williams, C., Shaw, B., Fry, B., & Nicol, A. (2024). Effects of subduction interface locking distributions on tsunami hazard: A case study on the Hikurangi/Tonga-Kermadec subduction zones. *Geophysical Journal International, 240*(2), 1147–1167. https://doi.org/10.1093/gji/ggae441

Hunter, J. D. (2007). Matplotlib: A 2D graphics environment. *Computing in Science & Engineering, 9*(3), 90–95. https://doi.org/10.1109/MCSE.2007.55

Lay, T., Kanamori, H., Ammon, C. J., Nettles, M., Ward, S. N., Aster, R. C., Beck, S. L., Bilek, S. L., Brudzinski, M. R., Butler, R., DeShon, H. R., Ekström, G., Satake, K., & Sipkin, S. (2005). The great Sumatra-Andaman earthquake of 26 December 2004. *Science, 308*(5725), 1127–1133. https://doi.org/10.1126/science.1112250

Lay, T. (2018). A review of the rupture characteristics of the 2011 Tohoku-Oki Mw 9.1 earthquake. *Tectonophysics, 733*, 4–36. https://doi.org/10.1016/j.tecto.2017.09.022

LeVeque, R. J., Waagan, K., González, F. I., Rim, D., & Lin, G. (2016). Generating random earthquake events for probabilistic tsunami hazard assessment. In E. L. Geist, H. M. Fritz, A. B. Rabinovich, & Y. Tanioka (Eds.), *Global tsunami science: Past and future, Volume I* (pp. 3671–3692). Springer International Publishing. https://doi.org/10.1007/978-3-319-55480-8_2

Mai, P. M., & Beroza, G. C. (2002). A spatial random field model to characterize complexity in earthquake slip. *Journal of Geophysical Research: Solid Earth, 107*(B11), 2308. https://doi.org/10.1029/2001JB000588

Melgar, D., Crowell, B. W., Geng, J., Allen, R. M., Bock, Y., Riquelme, S., Hill, E. M., Protti, M., & Ganas, A. (2015). Earthquake magnitude calculation without saturation from the scaling of peak ground displacement. *Geophysical Research Letters, 42*(13), 5197–5205. https://doi.org/10.1002/2015GL064278

Melgar, D., LeVeque, R. J., Dreger, D. S., & Allen, R. M. (2016). Kinematic rupture scenarios and synthetic displacement data: An example application to the Cascadia subduction zone. *Journal of Geophysical Research: Solid Earth, 121*(9), 6658–6674. https://doi.org/10.1002/2016JB013314

Melgar, D., & Hayes, G. P. (2017). Systematic observations of the slip pulse properties of large earthquake ruptures. *Geophysical Research Letters*, *44*(19), 9691–9698. https://doi.org/10.1002/2017GL074916

Melgar, D., & Hayes, G. P. (2019). The correlation lengths and hypocentral positions of great earthquakes. *Bulletin of the Seismological Society of America, 109*(6), 2582–2593. https://doi.org/10.1785/0120190164

Melgar, D., Crowell, B. W., Melbourne, T. I., Szeliga, W., Santillan, M., & Scrivner, C. (2020). Noise characteristics of operational real-time high-rate GNSS positions in a large aperture network. *Journal of Geophysical Research: Solid Earth, 125*(7), e2019JB019197. https://doi.org/10.1029/2019jb019197

Mena, B., Mai, P. M., Olsen, K. B., Purvance, M. D., & Brune, J. N. (2010). Hybrid broadband ground-motion simulation using scattering Green's functions: Application to large-magnitude events. *Bulletin of the Seismological Society of America, 100*(5A), 2143–2162. https://doi.org/10.1785/0120080318

Mori, N., Takahashi, T., Yasuda, T., & Yanagisawa, H. (2011). Survey of 2011 Tohoku earthquake tsunami inundation and run-up. *Geophysical Research Letters, 38*(7), L00G05. https://doi.org/10.1029/2011GL049210

Murray, J. R., Crowell, B. W., Murray, M. H., Ulberg, C. W., McGuire, J. J., Aranha, M. A., & Hagerty, M. T. (2023). Incorporation of real-time earthquake magnitudes estimated via peak ground displacement scaling in the ShakeAlert earthquake early warning system. Bulletin of the Seismological Society of America, 113(3), 1286–1310. https://doi.org/10.1785/0120220181

Nye, T., Sahakian, V., & Melgar, D. (2024). Modeling ground motions and crustal deformation from tsunami earthquakes: Rupture parameter constraints from the 2010 Mentawai event. *Seismica, 3*(2). https://doi.org/10.26443/seismica.v3i2.1152

Orchiston, C., Mitchell, J., Wilson, T., Langridge, R., Davies, T., Bradley, B., Johnston, D., Davies, A., Becker, J., & McKay, A. (2018). Project AF8: Developing a coordinated, multi-agency response plan for a future great Alpine Fault earthquake. *New Zealand Journal of Geology and Geophysics, 61*(3), 389–402. https://doi.org/10.1080/00288306.2018.1455716

Ozawa, S., Ida, A., Hoshino, T., & Ando, R. (2022). Large-scale earthquake sequence simulations on 3-D non-planar faults using the boundary element method accelerated by lattice H-matrices. *Geophysical Journal International*, *232*(3), 1471–1481. https://doi.org/10.1093/gji/ggac386

Rafiei, M., Khodaverdian, A., & Rahimian, M. (2022). A probabilistic physics-based seismic hazard model for the Alborz Region, Iran. *Bulletin of the Seismological Society of America, 112*(4), 2141–2155. https://doi.org/10.1785/0120210238

Richards-Dinger, K., & Dieterich, J. H. (2012). RSQSim earthquake simulator. *Seismological Research Letters, 83*(6), 983–990. https://doi.org/10.1785/0220120105

Ruhl, C. J., Melgar, D., Grapenthin, R., & Allen, R. M. (2017). The value of real-time GNSS to earthquake early warning. *Geophysical Research Letters, 44*(16), 8311–8319. https://doi.org/10.1002/2017GL074502

Shaw, B. E., Milner, K. R., Field, E. H., Richards-Dinger, K., Gilchrist, J. J., Dieterich, J. H., & Jordan, T. H. (2018). A physics-based earthquake simulator replicates seismic hazard statistics across California. Science Advances, 4(8), eaau0688. https://doi.org/10.1126/sciadv.aau0688

Shaw, B. E., Fry, B., Nicol, A., Howell, A., & Gerstenberger, M. (2022). An earthquake simulator for New Zealand. *Bulletin of the Seismological Society of America, 112*(2), 763–778. https://doi.org/10.1785/0120210087

Small, D. T., & Melgar, D. (2023). Can stochastic slip rupture modeling produce realistic M9+ events? *Journal of Geophysical Research: Solid Earth, 128*(3), e2022JB025716. https://doi.org/10.1029/2022JB025716

Solares-Colón, M. M., Melgar, D., Howell, A., Crowell, B., D'Anastasio, E., Caballero, E., & Fry, B. (2025). Using ruptures from earthquake cycle simulators to test geodetic early warning systems performance (Supplementary Data) [Data set]. Zenodo. https://doi.org/10.5281/zenodo.15522298

Stirling, M., Fitzgerald, M., Shaw, B., & Ross, C. (2024). New magnitude–area scaling relations for the New Zealand National Seismic Hazard Model 2022. *Bulletin of the Seismological Society of America, 114*(1), 137–149. https://doi.org/10.1785/0120230114

Tian, D., Uieda, L., Leong, W. J., Fröhlich, Y., Schlitzer, W., Grund, M., Jones, M., Toney, L., Yao, J., Magen, Y., Tong, J.-H., Materna, K., Belem, A., Newton, T., Anant, A., Ziebarth, M., Quinn, J., & Wessel, P. (2024). PyGMT: A Python interface for the Generic Mapping Tools (v0.12.0). Zenodo. https://doi.org/10.5281/zenodo.11062720

Uphoff, C., May, D. A., & Gabriel, A.-A. (2022). A discontinuous Galerkin method for sequences of earthquakes and aseismic slip on multiple faults using unstructured curvilinear grids. *Geophysical Journal International, 233*(1), 586–626. https://doi.org/10.1093/gji/ggac467

Van Dissen, R. J., Johnson, K. M., Seebeck, H., Wallace, L. M., Rollins, C., Maurer, J., Gerstenberger, M. C., Williams, C. A., Hamling, I. J., Howell, A., & DiCaprio, C. J. (2024). Upper plate and subduction interface deformation models in the 2022 revision of the Aotearoa New Zealand National Seismic Hazard Model. *Bulletin of the Seismological Society of America, 114*(1), 37–56. https://doi.org/10.1785/0120230118

Vargas, G., Farías, M., Carretier, S., Tassara, A., Baize, S., & Melnick, D. (2011). Coastal uplift and tsunami effects associated with the 2010 Mw8.8 Maule earthquake in central Chile. *Andean Geology, 38*(1), 219–238.

Wallace, L. M. (2020). Slow slip events in New Zealand. *Annual Review of Earth and Planetary Sciences, 48*(1), 175–203. https://doi.org/10.1146/annurev-earth-071719-055104

Williams, C. A., Eberhart-Phillips, D., Bannister, S., Barker, D. H. N., Henrys, S., Reyners, M., & Sutherland, R. (2013). Revised interface geometry for the Hikurangi Subduction Zone, New Zealand. *Seismological Research Letters, 84*(6), 1066–1073. https://doi.org/10.1785/0220130035

Williamson, A. L., Melgar, D., Crowell, B. W., Arcas, D., Melbourne, T. I., Wei, Y., & Kwong, K. (2020). Toward near-field tsunami forecasting along the Cascadia subduction zone using rapid GNSS source models. *Journal of Geophysical Research: Solid Earth, 125*(8), e2020JB019636. https://doi.org/10.1029/2020JB019636

Yue, H., Lay, T., Rivera, L., An, C., Vigny, C., Tong, X., & Báez Soto, J. C. (2014). Localized fault slip to the trench in the 2010 Maule, Chile (Mw 8.8) earthquake from joint inversion of high-rate GPS, teleseismic body waves, InSAR, campaign GPS, and tsunami observations. *Journal of Geophysical Research: Solid Earth, 119*(10), 7786–7804. https://doi.org/10.1002/2014JB011340

Zhu, L., & Rivera, L. A. (2002). A note on the dynamic and static displacements from a point source in multilayered media: A note on the dynamic and static displacements from a point source. *Geophysical Journal International, 148*(3), 619–627. https://doi.org/10.1046/j.1365-246X.2002.01610.x

Zielke, O., & Mai, P. M. (2023). MCQsim: A multicycle earthquake simulator. *Bulletin of the Seismological Society of America, 113*(3), 889–908. https://doi.org/10.1785/0120220248

Seismica

Supporting Information for

Using ruptures from an earthquake cycle simulator to test geodetic early warning system performance

M. M. Solares-Colón[1], D. Melgar[1], A. Howell[2], B. Crowell[3], E. D'Anastasio[2], E. Caballero[2], and B. Fry[2]

[1]Department of Earth Sciences, University of Oregon, Eugene, Oregon, U.S.A.
[2] Earth Sciences New Zealand Te Pū Ao, Lower Hutt, Aotearoa, New Zealand
[3]School of Earth Sciences, The Ohio State University, Columbus, Ohio, U.S.A.

Contents of this file

Introduction

This supplement contains auxiliary information on methods and results. Table S1 (modified from Hughes et al., 2024) provides input parameters used in Rate and State Earthquake Simulator (RSQSim; Richards-Dinger & Dieterich, 2012) to generate rupture scenario catalog. Table S2 (modified from Goldberg et al., 2021) provides the GNSS Ground Motion Model coefficients used for waveform validation and for testing the Geodetic First Approximation of Size and Timing (G-FAST; Crowell et al., 2016, Crowell et al., 2018) early earthquake warning algorithm in this study. Figure S1 shows the spatial distribution and magnitude range of events from both catalogs, RSQSim and FakeQuakes, used in this study. Figure S2 illustrates the discrepancies between hypocenters and centroids for each rupture scenario, comparing the original rupture locations with geodetic CMT estimates from G-FAST.Figure S3 highlights an extraordinary case of a full-rupture event in the Kermadec-Tonga subduction system, where G-FAST was unable to produce a solution.

Model Parameter	**$Trench_{Lock}$ Value**
Rate and state (*a* value)	0.001
Rate and state (*b* value)	0.004
Coefficient of friction (μ_0)	0.6
Rate and state (D_c)	$1x10^{-5}$
Rate and state (α_0)	0.25
Rate and state (θ_0)	$2x10^{8}$
Initial shear stress (τ_0)	60
Initial normal stress (σ_0)	100
Slip-deficit Model (HSM)	Trench creep model used in the NSHM 2022
Slip-deficit Model (TKSZ)	20% of the plate rate between ~37˚S to ~29˚S, and 50% of the plate rate from ~29˚S to ~25˚S

Table S1. Summary of the input parameters in RSQSim used to generate rupture scenario catalog (for details refer to Hughes et al., 2024); Hikurangi Subduction Margin (HSM); New Zealand National Seismic Hazard Model 2022 (NSHM 2022); Tonga-Kermadec Subduction Zone (TKSZ).

Study	A	B	C
Crowell et al. (2016)*	-6.687	1.500	-0.214
Goldberg et al. (2021)**	-3.841	0.937	-0.127

** Crowell et al. (2016) PGD scaling uses hypocentral distance and applies exponential distance weighting to favor stations closer to the source.*
*** Goldberg et al. (2021) PGD scaling uses generalized mean rupture distance.*

Table S2. GNSS Ground Motion Model coefficients for waveform validation and G-FAST testing. For waveform validation we use Goldberg et al. (2021) using the generalized mean rupture distance, R_p, with a value of – 2.3 for the power of the mean (p). The advantage of using R_p as a distance metric is that it allows for a more realistic treatment of a finite source as opposed to assuming a large rupture is a point source (e.g. as with the hypocenter distance; for more details refer to Goldberg et al. 2021). G-FAST PGD scaling applies exponential weighting as a function of epicentral distance to prioritize stations closer to the source, using a minimum of four stations and a 3 km/s travel-time mask to exclude those that have not yet experienced strong ground shaking, enabling rapid characterization of large events (for more details refer to Crowell et al., 2016).

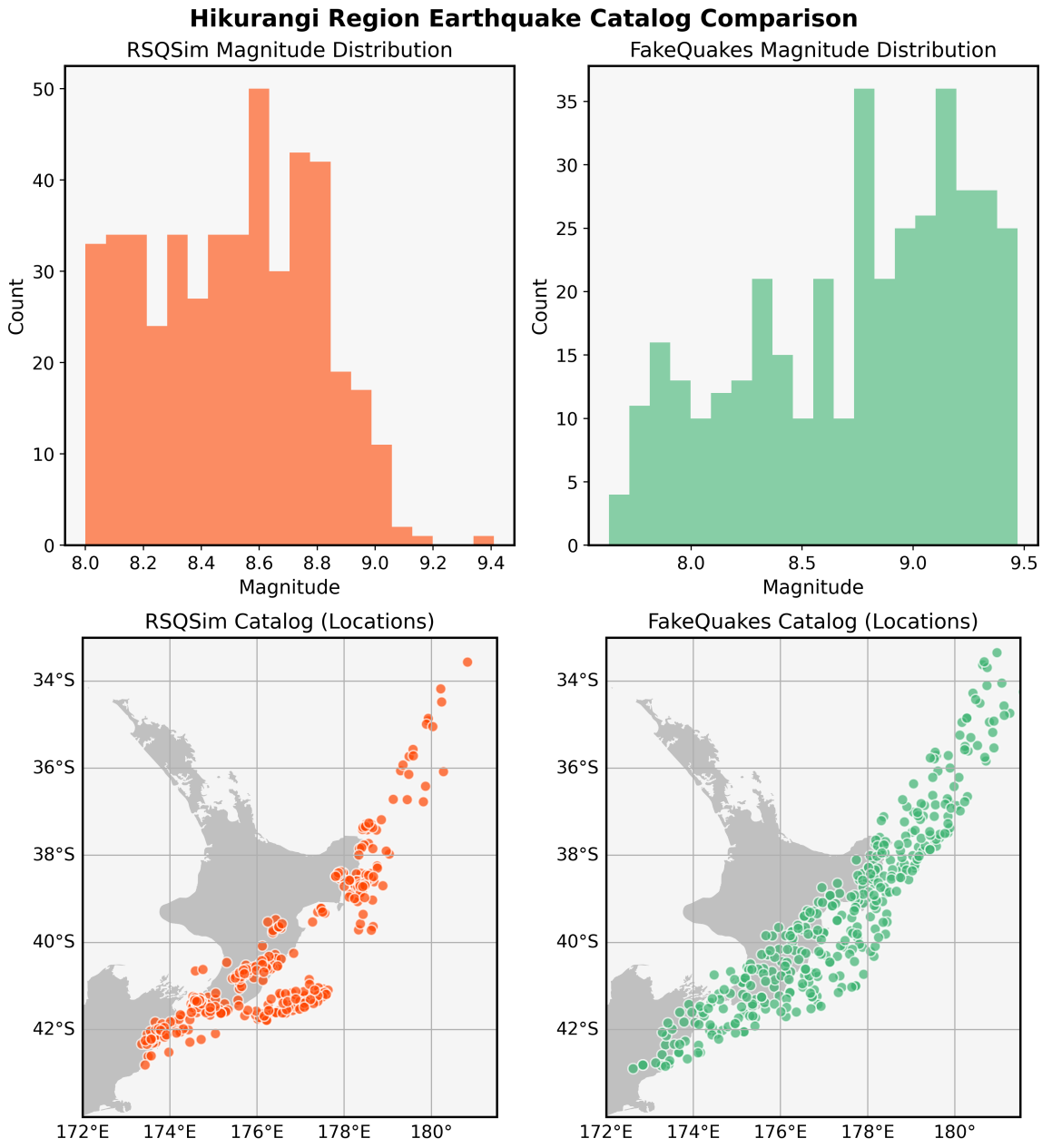

Figure S1. Comparison of the two synthetic earthquake catalogs for New Zealand: RSQSim (in orange) and FakeQuakes (in green). Top panels show the magnitude distribution of earthquakes (histograms) for each catalog, while bottom panels show the spatial distribution of earthquakes (epicenters represented by circles) over the Hikurangi region. Both catalogs exhibit a similar geographic extent but show differences in event density and magnitude distributions that reflect variations in catalog generation methods. RSQSim represents a long-term synthetic seismicity history based on physics-based modeling, whereas FakeQuakes provides a more comprehensive suite of rupture scenarios designed to explore a wide range of magnitudes and locations.

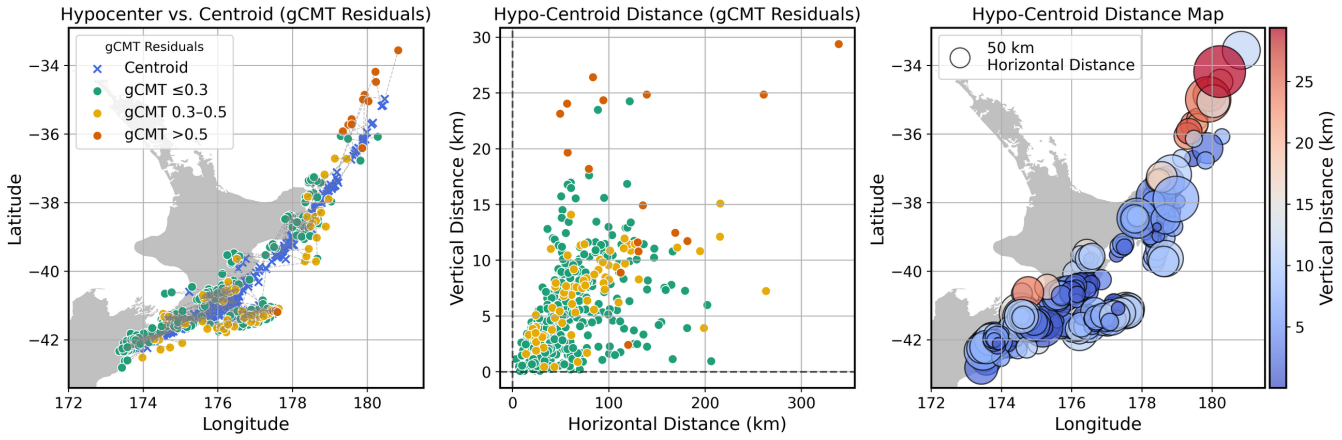

Figure S2. Comparison of hypocenter and centroid locations with magnitude residual (Final – Target) categories for geodetic centroid moment tensor (gCMT) solutions. The left panel shows hypocenter locations (circles) and centroid locations (blue crosses) for gCMT residuals. Hypocenter locations are color-coded by error magnitude: green for low errors (≤0.3), yellow for moderate errors (0.3–0.5), and red for large errors (>0.5), corresponding to varying residual magnitudes. Centroid estimates from G-FAST are shown as white stars for comparison. The middle panel presents hypocenter vs. centroid locations for gCMT residuals, following the same residual categorization. The right panel displays a hypocenter map, where marker size and color represent the horizontal and vertical distances, respectively, between the hypocenter and centroid.

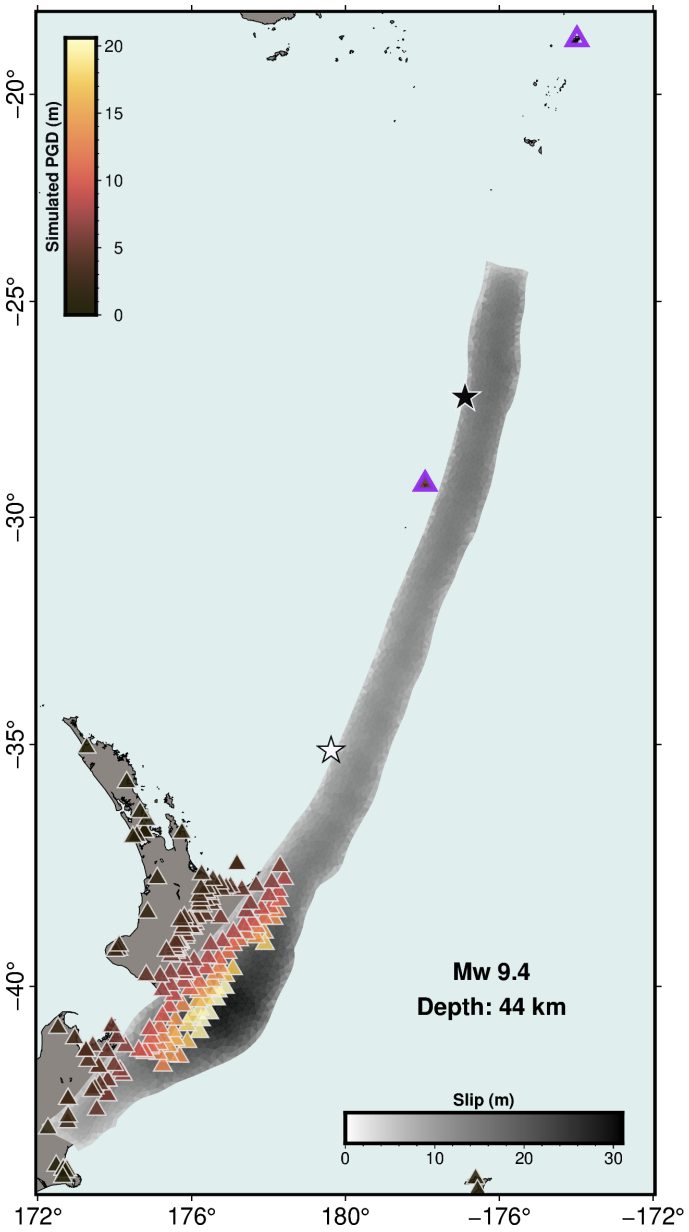

Figure S3. An extraordinary case of a full-rupture **M**9.4 event in the Kermadec-Tonga subduction system, where G-FAST is unable to produce a solution because the stations are too far from the hypocenter to compute a reliable estimate. The map shows observed peak ground displacement (PGD) values at each station (color-filled triangles) within 1000 km, based on the distance from the station to the entire rupture plane (R_p), shown in warm colors. The grayscale colormap represents the amount of rupture slip for reference. Triangles with thick purple borders indicate stations within 1000 km based on the distance from the station to the hypocenter (R_{hypo}). The black star shows the hypocenter, while the white star represents the centroid location. Labels indicate the magnitude and depth of the event.

References

Crowell, B. W., Schmidt, D. A., Bodin, P., Vidale, J. E., Gomberg, J., Hartog, J. R., Kress, V. C., Melbourne, T. I., Santillan, M., Minson, S. E., & Jamison, D. G. (2016). Demonstration of the Cascadia G-FAST geodetic earthquake early warning system for the Nisqually, Washington, earthquake. *Seismological Research Letters, 87*(4), 930–943. https://doi.org/10.1785/0220150255

Crowell, B. W., Schmidt, D. A., Bodin, P., Vidale, J. E., Baker, B., Barrientos, S., & Geng, J. (2018). G-FAST earthquake early warning potential for great earthquakes in Chile. *Seismological Research Letters, 89*(2A), 542–556. https://doi.org/10.1785/0220170180

Hughes, L., Lane, E. M., Power, W., Savage, M. K., Arnold, R., Howell, A., Liao, Y.-W. M., Williams, C., Shaw, B., Fry, B., & Nicol, A. (2024). Effects of subduction interface locking distributions on tsunami hazard: A case study on the Hikurangi/Tonga-Kermadec subduction zones. *Geophysical Journal International, 240*(2), 1147–1167. https://doi.org/10.1093/gji/ggae441

Goldberg, D. E., Melgar, D., Hayes, G. P., Crowell, B. W., & Sahakian, V. J. (2021). A ground-motion model for GNSS peak ground displacement. *Bulletin of the Seismological Society of America, 111*(5), 2393–2407. https://doi.org/10.1785/0120210042

Richards-Dinger, K., & Dieterich, J. H. (2012). RSQSim earthquake simulator. *Seismological Research Letters, 83*(6), 983–990. https://doi.org/10.1785/0220120105